RESEARCH LETTER

Cryo-EM structure of a novel α-synuclein filament subtype from multiple system atrophy

Nicholas L. Yan[1] (iD), Francisco Candido[1], Eric Tse[1,2] (iD), Arthur A. Melo[1] (iD), Stanley B. Prusiner[1,2,3] (iD), Daniel A. Mordes[1,4,5] (iD), Daniel R. Southworth[1,3] (iD), Nick A. Paras[1,2] (iD) and Gregory E. Merz[1,2] (iD)

1 Institute for Neurodegenerative Diseases, Weill Institute for Neurosciences, University of California San Francisco, CA, USA
2 Department of Neurology, Weill Institute for Neurosciences, University of California San Francisco, CA, USA
3 Department of Biochemistry and Biophysics, University of California San Francisco, CA, USA
4 Department of Pathology, University of California San Francisco, CA, USA
5 Department of Pathology, Massachusetts General Hospital, Boston, MA, USA

Multiple system atrophy (MSA) is a progressive neurodegenerative disease characterized by accumulation of α-synuclein cross-β amyloid filaments in the brain. Previous structural studies of these filaments by cryo-electron microscopy (cryo-EM) revealed three discrete folds distinct from α-synuclein filaments associated with other neurodegenerative diseases. Here, we use cryo-EM to identify a novel, low-populated MSA filament subtype (designated Type I_2) in addition to a predominant class comprising MSA Type II_2 filaments. The 3.3-Å resolution structure of the Type I_2 filament reveals a fold consisting of two asymmetric protofilaments, one of which adopts a novel structure that is chimeric between two previously reported protofilaments. These results further define MSA-specific folds of α-synuclein filaments and have implications for designing MSA diagnostics and therapeutics.

Keywords: cryo-electron microscopy; multiple system atrophy; neurodegeneration; prion; protein aggregation; α-synuclein

α-Synuclein is an intrinsically disordered, 140–amino acid protein [1] that localizes primarily to the axon terminals of presynaptic neurons, where it participates in membrane binding, vesicle trafficking, and neurotransmitter release [2,3]. The misfolding and aggregation of α-synuclein in the brain are hallmarks of a group of neurodegenerative diseases known as synucleinopathies [4,5], which includes Parkinson's disease and dementia with Lewy bodies. One such disease, multiple system atrophy (MSA), is clinically characterized by cerebellar dysfunction or parkinsonism and neuropathologically characterized by glial cytoplasmic inclusions (GCIs) in oligodendrocytes [6,7]. GCIs contain abundant fibrils that appear to be the result of soluble α-synuclein misfolding into self-templating prion conformations that ultimately misassemble as insoluble amyloid filaments [8–12]. Structural studies on filaments isolated from five MSA patients revealed three distinct filament types (denoted Type I, II_1, and II_2). These findings contrast with Lewy body pathologies, which appear to contain a single α-synuclein filament type, and juvenile-onset synucleinopathy, which contains one α-synuclein fold in either a singlet or doublet association [13–15].

The previously determined MSA filament types each consist of two asymmetric protofilaments (PF-A and PF-B) that associate along an extended interface nearly spanning the width of the filament core (Fig. S1) [13].

Also common to each type is a central channel flanked by basic residues (Lys43, Lys45, and His50 of each protofilament) with unassigned density present within the channel. However, major conformational differences lie within the protofilaments that compose each mature fibril core. Type I MSA filaments contain two PFs, one PF-IA and one PF-IB. Residues Gly14 to Phe94 are resolved in PF-IA, and Lys21 to Gln99 are resolved in PF-IB. While both PF-IA and PF-IB contain a hairpin motif in the N-terminal region and a three-layered L-shaped motif in the C-terminal region, PF-IA also contains a single-layered L-shaped motif (residues 32–45) joining the N- and C-terminal motifs. Thus, the residues composing the terminal motifs differ in each protofilament, and the fold of the three-layered L-shaped motif also differs in the packing of the inner layer relative to the central layer.

The Type II filament subtypes (II_1 and II_2) each have two protofilaments [13] and contain identical PF-IIA, which span residues 14–94. Comparing PF-IA and PF-IIA, the N-terminal regions spanning residues 14–42 are conformationally identical. However, these protofilaments differ in the C-terminal region, including the conformation of the three-layered L-shaped motif. PF-IIA contains a small channel within the filament core, surrounded by Val52, Thr54, Ala56, Thr59, Glu61, Thr72, Gly73, and Val74, that is not present in PF-IIB because these residues form closer contacts with each other. $PF-IIB_1$ and $PF-IIB_2$ include residues 36–99 and contain a three-layered L-shaped motif (residues 47–99). In contrast to PF-IB, these protofilaments lack the N-terminal hairpin and contain a shorter single-layered L-shaped motif (residues 36–46) instead. $PF-IIB_1$ and $PF-IIB_2$ are distinguished from each other by a change in a surface loop at the C-terminal end of the ordered core (residues 81–90). The surface loop conformation of $PF-IIB_1$ is similar to the loop in PF-IB, while $PF-IIB_2$ has a distinct loop conformation that is shifted approximately 4 Å toward the C terminus of the protofilament core. The overall helical symmetry of each MSA filament type is similar, although Type I filaments have a slightly greater twist (−1.42°) compared to Type II_1/II_2 filaments (−1.34°).

MSA filament types are heterogeneously distributed between different patients [13]. For example, in the original report from Schweighauser et al., two patients had almost exclusively Type I filaments, one patient had almost exclusively Type II filaments, and the remaining two patients had both Type I and II filaments in varying ratios. This heterogeneity suggests that there may be a greater variety of folds than previously reported. In this study, we use cryo-EM to obtain high-resolution (3.2–3.3 Å) structures of

filaments purified from tissue of another patient with MSA. While the majority (66%) of the data consists of Type II_2 filaments, our results reveal a novel protofilament subtype in a subset (5%) of filaments that are related to Type I filaments.

Materials and methods

MSA filament extraction

Deidentified human tissue was obtained from the Massachusetts Alzheimer's Disease Research Center (ADRC). All donors provided consent to donate brains for research purposes in accordance with the standards of the ADRC. This study was exempt from institutional review board approval in accordance with the institutional review board policy of the University of California San Francisco. Filament extraction was performed using a modified protocol from Schweighauser et al. [13]. In summary, 1–2 g of freshly frozen cerebellum tissue from a patient pathologically diagnosed with MSA was homogenized at 20 mL·g^{-1} of tissue in 10 mM Tris-HCl (pH 7.4), 800 mM NaCl, 1 mM EGTA, and 10% sucrose. N-lauroylsarcosinate (final concentration of 1% w/v) was added to the homogenate and incubated at 37 °C for 30 min. Afterward, homogenates were centrifuged at 10 000 *g* for 10 min. The supernatant was kept and centrifuged at 100 000 *g* for 20 min. The pellet was resuspended at 500 μL·g^{-1} of frozen tissue in 10 mM Tris-HCl (pH 7.4), 800 mM NaCl, 1 mM EGTA, and 10% sucrose. The suspension was then centrifuged at 3000 *g* for 5 min. The supernatant was kept and diluted threefold with 50 mM Tris-HCl (pH 7.4), 150 mM NaCl, 10% sucrose, and 2% sarkosyl. This suspension was then centrifuged at 150 000 *g* for 1 h. The filament-enriched pellet was resuspended in 30 mM Tris-HCl (pH 7.4) using 100 μL·g^{-1} of frozen tissue.

Cryo-EM sample preparation and data collection

Purified filaments (3 μL) were added to a 200 mesh 1.2/1.3R Au Quantifoil grid coated with a 2-nm thick carbon layer, which was not glow discharged. After 30 s, grids were blotted for 7.5 s at room temperature and 100% humidity using a FEI Vitrobot Mark IV, followed by plunge freezing in liquid ethane. A total of 42 224 super-resolution movies were collected at a nominal magnification of 105 000× (physical pixel size: 0.417 Å/pixel) on a Titan Krios (Thermo Fisher Scientific, Waltham, MA) operated at 300 kV and equipped with a K3 direct electron detector and BioQuantum energy filter (Gatan, Inc., Pleasanton, CA) set to a slit width of 20 eV. A defocus range of −0.8 to −1.8 μm was used with a total exposure time of 2.024 s fractionated into 0.025-s subframes. The total dose for each movie was 46 electrons/Å^2. Movies were motion corrected using MotionCor2 [16] in Scipion [17] and were

Fourier cropped by a factor of 2 to a final pixel size of 0.834 Å/pixel. Motion-corrected and dose-weighted micrographs were manually curated in Scipion to remove micrographs lacking filaments, those at low resolution, or those with significant ice contamination, resulting in 4392 remaining micrographs.

Cryo-EM image processing

A graphical overview of the data processing workflow is provided in Fig. S2. All image processing was done in RELION 4 [18,19]. Dose-weighted summed micrographs were imported into RELION 4. The contrast transfer function was estimated using CTFFIND-4.1 [20]. Filaments were manually picked, and segments were extracted with a box size of 900 pixels downscaled to 300 pixels, resulting in 257 982 segments. Reference-free 2D classification was used to remove contaminants and segments contributing to straight filaments, resulting in 255 032 remaining segments. These were re-extracted with a box size of 288 pixels without downscaling, followed by another round of reference-free 2D classification that did not filter out more contaminant segments. One round of 3D classification with image alignment was performed on the segments using a reference map consisting of the existing MSA Type I filaments (PDB code: 6XYO), a regularization parameter (T) of 20, and fixing helical parameters to $-1.42°$ twist and 4.76 Å rise. We were unable to resolve Type I_2 filaments by allowing the helical parameters to vary. One class (12 802 segments) corresponded to Type I_2 filaments. One round of 3D auto-refinement was run using this map low-pass filtered to 10 Å, allowing rise and twist parameters to vary. The map was sharpened using the standard postprocessing procedures in RELION. Full statistics are shown in Table S1.

Two out of the 12 classes (57 809 segments) corresponded to Type II_2 filaments with no breaks in the polypeptide density. Segments corresponding to these classes were pooled and subjected to one round of 3D classification without image alignment using a reference map consisting of one of these classes (A3; Fig. S3), a regularization parameter (T) of 20, and fixing helical parameters to $-1.34°$ twist and 4.76 Å rise. The highest resolution class (31 115 segments) was subjected to 3D auto-refinement and postprocessing to give a refined Type II_2 filament map.

Of the 12 classes, 4 classes (110 255 segments) displayed clear separation between protofilaments in the z-direction but modest resolution in the x- and y-directions, suggesting suboptimal alignment. Segments corresponding to these classes were pooled and subjected to one round of 3D classification with image alignment using a reference map consisting of the existing MSA Type II_2 filaments (PDB code: 6XYQ), a regularization parameter (T) of 20, and fixing helical parameters to $-1.34°$ twist and 4.76 Å rise. Most of these segments (110 071) converged into one class

corresponding to Type II_2 filaments, which was not further refined. The remaining classes (74 166 segments) from the initial round of 3D classification were low resolution and excluded from further processing.

To eliminate bias in 3D classification and further verify the distribution of filaments, we generated a 3D initial model ab initio from 2D class averages using RELION's relion_helix_inimodel2d feature. This initial model was used as a reference map for 3D classification using the otherwise same inputs as the first round of 3D classification described above, resulting in classes corresponding to Type II_2 filaments (206 869 segments, 81% of the data) and Type I_2 filaments (15 369 segments, 6% of the data).

Model building, refinement, and analysis

A single strand of the previously solved MSA Type II_2 (PDB code: 6XYQ) or Type I (PDB code: 6XYO) filament structures was placed in the density using Chimera [21]. Subsequent model building was performed using COOT [22] and ISOLDE [23] followed by refinement in PHENIX [24]. The model was then translated to produce a stack occupying all regions with continuous density on the map. Refinement statistics are shown in Table S1. Data were deposited into the Protein Data Bank (PDB) under accession codes 9CD9 (Type II_2) and 9CDA (Type I_2) and into the Electron Microscopy Data Bank (EMDB) under accession codes EMD-45464 (Type II_2) and EMD-45465 (Type I_2).

Results

Partially purified, sarkosyl-insoluble filaments were isolated from the postmortem cerebellum of a 67-year-old male neuropathologically diagnosed with MSA. Negative-stain transmission electron microscopy on this sample revealed filaments that were morphologically similar to those in previous reports (Fig. S4) [13,25]. After cryo-EM imaging using standard collection methods (Fig. 1A; see 'Materials and methods'), reference-free 2D classification resulted in 2D class averages that were similar to those previously reported [13], exhibiting a crossover distance of approximately 600 Å (Fig. S5). However, it was unclear whether these 2D classes corresponded to a known filament type. After 3D classification and helical reconstruction, we were able to obtain high-resolution structures of two MSA filament types (Fig. 1B). The primary type (Fig. 1C), refined to 3.2 Å and representing 66% of the data (Table S1), was nearly identical to Type II_2 filaments (PDB: 6XYQ), with an all-atom root-mean-square deviation (RMSD) of 0.5 Å (Fig. S6). We observed previously reported regions of unknown density, such as non-proteinaceous density within the
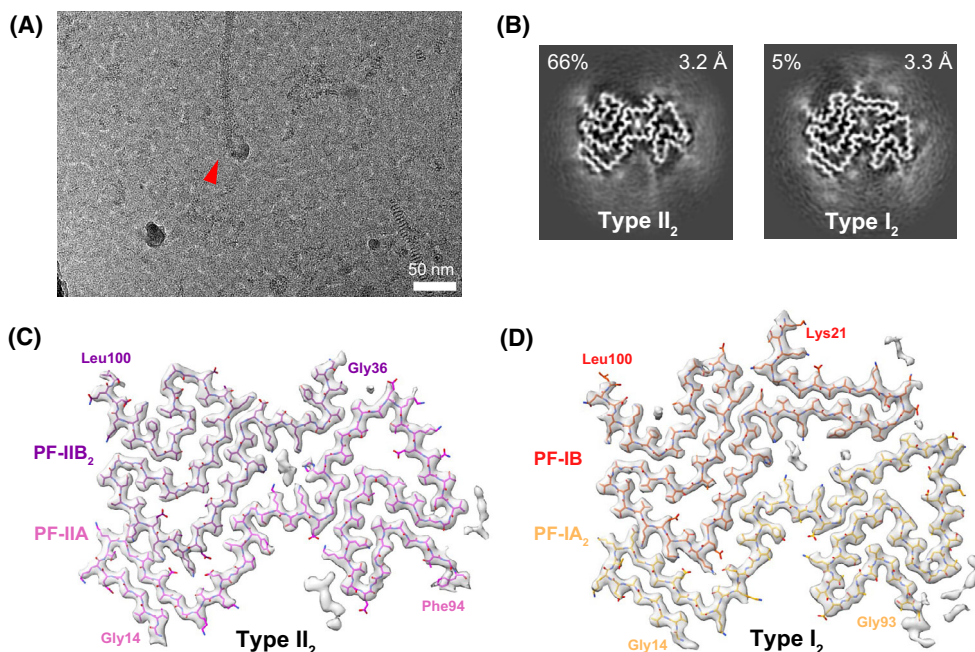
Fig. 1. Cryo-EM analysis of *ex vivo* MSA filaments reveals a novel filament subtype: Type I_2 filaments. (A) Representative micrograph. The red arrow indicates an MSA filament. (B) Cross section of two major conformations of MSA filaments, Type II_2 and Type I_2, identified after 3D classification of filament segments. The resolutions of the final reconstructions and abundance in the data are indicated. The remaining 29% of data consisted of low-resolution classes. (C) Density map and model of Type II_2 filaments. The two constituent protofilaments PF-IIA and PF-IIB$_2$, along with residues at the termini of the ordered core, are labeled and color coded in pink and purple, respectively. Regions of unmodeled density are also shown. (D) Density map and model of Type I_2 filaments. The two constituent protofilaments PF-IA$_2$ and PF-IB, along with residues at the termini of the ordered core, are labeled and color coded in yellow and red, respectively. Regions of unmodeled density are also shown.

central channel flanked by basic residues and a peptide-like density contacting residues Lys80-Val82 of PF-IIA [13]. We were able to resolve an additional residue (Leu100) at the C-terminal region of the PF-IIB$_2$ ordered core.

In addition to the successful reproduction of the Type II_2 MSA filament, we also resolved a filament exhibiting a conformation of α-synuclein that has not been reported previously. We refer to this low-populated filament subtype as a Type I_2 filament, which represents 5% of the data (Fig. 1B, Fig. S7). The structure of Type I_2 filaments, refined to 3.3-Å resolution, resembles Type I (hereafter called Type I_1) and comprises two protofilaments, PF-IA$_2$ and PF-IB (Fig. 1D). The ordered core of these protofilaments includes residues Gly14-Gly93 for PF-IA$_2$ and Lys21-Leu100 for PF-1B. The PF-IB protofilament is common between Type I_1 and Type I_2 filaments, with an RMSD of 0.8 Å to the existing Type I_1 filament model (PDB: 6XYO) [13].

The differences between Type I_1 and Type I_2 filaments exist within the second protofilament: PF-IA for Type I_1 and PF-IA$_2$ for Type I_2 (Fig. 2A). While the

N-terminal regions comprising residues 14–56 are nearly identical between the two protofilaments, the C-terminal regions of the protofilaments (residues 57–93) adopt distinct conformations. Specifically, this region in PF-IA$_2$ is shifted outwards and away from the inter-protofilament interface. This conformational change shifts the register of the hydrophobic intraprotofilament interface containing residues Val74 and Ala76 by two residues and creates a channel within the filament core, resulting in a net loss of hydrophobic interactions, including those made by the Val52 and Thr54 sidechains (Fig. 2B). Additionally, potential interstrand polar contacts between the Glu61 sidechain and Gly73 backbone amide are lost. Interestingly, the C-terminal region of PF-IA$_2$ is virtually identical to the analogous region in PF-IIA found within Type II MSA filaments, although PF-IIA contains the C-terminal Phe94 residue that was not well resolved in PF-IA$_2$ (Fig. 2C). Comparing PF-IA and PF-IA$_2$, the average Cα displacement of residues 57–93 is 4.8 Å but is 0.3 Å between PF-IIA and PF-IA$_2$. Just as in PF-IIA, no additional, non-proteinaceous densities are observed in the C-terminal channel of PF-IA$_2$.
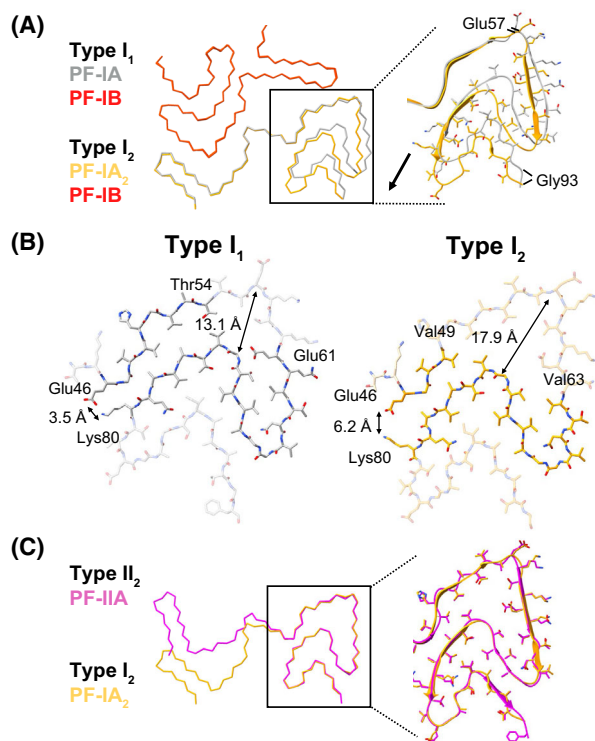
Fig. 2. Comparison of MSA Type I_2 filaments to previously solved MSA filament structures. (A) Overlay of Type I_1 (PDB: 6XYO) and Type I_2 filaments aligned using PF-IB. The black arrow indicates the direction of the conformational change in the C-terminal region. The average Cα displacement of residues 57–93 is 4.8 Å. (B) Comparison of intraprotofilament contacts in the C-terminal regions of PF-IA (Type I_1) and PF-IA$_2$ (Type I_2). (C) Overlay of Type I_2 and Type II_2 (PDB: 6XYQ) filaments aligned using residues 47–93 of PF-IIA. For clarity, PF-1B and PF-IIB$_2$ are not shown.

The morphological and helical parameter similarities between Type II_2 and Type I_2 MSA filaments prompted us to inquire whether both types could coexist within the same filament or if the types are instead segregated to individual filaments. Previous cryo-EM analysis of amyloid filaments suggested that multiple morphologies and folds could coexist within the same filaments [14,26]. To address this question, we mapped segments classifying Type I_2 or Type II_2 conformations to the original micrographs (Fig. 3A–C). Due to the 13-fold greater abundance of Type II_2 compared to Type I_2 segments in the dataset, we only analyzed micrographs containing at least one Type I_2 segment, corresponding to 437 micrographs out of 4392 (10%). We found that 71% of the 556 filaments in these micrographs contained segments that classified exclusively or predominantly (90% or higher) to either Type I_2 or Type II_2 (Fig. 3D). The remaining minority of filaments contained a more mixed distribution of types, although Type I_2 tended to predominate (e.g., Fig. 3A). These results suggest that each

MSA type preferentially segregates into separate filaments, though it is possible that a small number of filaments contain mixed types. A precise quantification of this dataset is complicated by the possibility of suboptimal classification, the extent of which is unknown.

Discussion

Cryo-EM studies have been instrumental in determining the structures of disease-associated amyloid fibrils from synucleinopathies and other neurodegenerative diseases [13,14,27–30]. Proteins associated with these diseases adopt numerous polymorphic folds that are associated with specific neurodegenerative diseases [31]. In some diseases, such as MSA, α-synuclein can adopt multiple distinct folds that are heterogeneously distributed between patients [13]. While Type I_1 and II_2 filaments appear to predominate in MSA, the lower-population type II_1 also exists within some patients. Here, we have expanded the spectrum of known MSA filament types to include a fourth subtype, Type I_2 filaments.

Type I_2 filaments share one protofilament fold (PF-IB) with Type I_1 filaments but differ in the PF-IA$_2$ protofilament, which instead bears similarities to the C-terminal region of the PF-IIA protofilament found in Type II filaments. The chimeric nature of PF-IA$_2$ suggests that common intermediates may exist in the misfolding and aggregation pathways of α-synuclein in MSA but then diverge, leading to multiple folds. The exact nature of these pathways and the relative contribution of each filament type to disease remains unknown. While MSA has two phenotypes—MSA-C (cerebellar) and MSA-P (parkinsonian) [32]—whether the identity and distribution of filament types correlates to phenotype remains undetermined. Schweighauser et al. previously analyzed 10 tissue samples across three brain regions (putamen, cerebellum, and frontal cortex) and five MSA patients, revealing a heterogeneous distribution of MSA filament types in different samples (Table S2). Even when considering our results, a possible relationship between brain region and MSA filament type cannot be determined due to the small number of samples; this remains an important open question. It also remains unclear whether different filament conformations in MSA may arise independently.

We found that MSA Type I_2 and II_2 filaments tended to segregate to individual filaments, but it is possible that a small number of filaments contain a mixed population of both types. These results contrast with previous analyses of morphologically similar filament folds. Lewy body α-synuclein filaments were found to contain a roughly even distribution of both
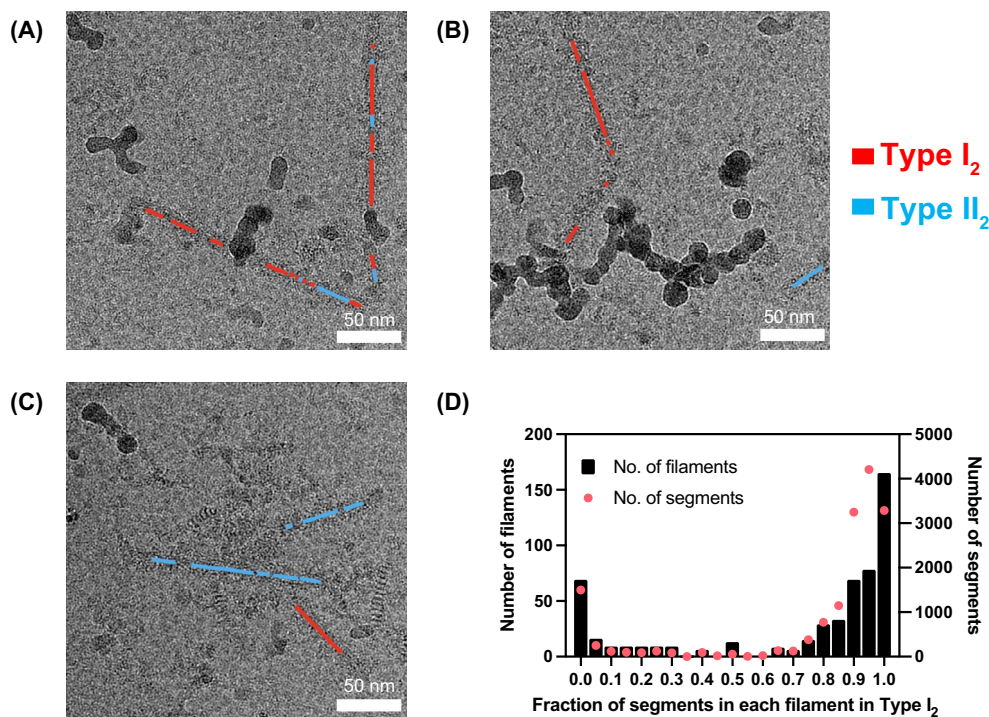
Fig. 3. Analysis of MSA Type I_2- and II_2-classified segments within individual filaments. (A–C) After one round of 3D classification, segments corresponding to either type were color coded and mapped to the original micrographs. (D) Histogram of the fraction of segments classified as Type I_2 per filament in micrographs containing at least one I_2 segment.

twisted and untwisted segments, although that analysis is limited by the lack of a structure of the untwisted morphology [14]. Another study investigating *ex vivo* antibody light chain filaments from a patient with systemic AL amyloidosis found two folds that unambiguously coexist in most filaments and differ only slightly in a surface-exposed region of the filament core [26]. The overall high homology allows for the formation of mixed filaments that maintain the favorable interstrand interactions needed for filament growth and stability. In the case of MSA Types I_2 and II_2, the folds are mostly dissimilar from each other except for residues 57–93 of PF-A, likely preventing the formation of a stable interface between both types. We attempted to model one Type I_2 filament rung directly adjacent to a Type II_2 filament rung, which were aligned using the homologous residues 57–93 of PF-IIA (Fig. S3). However, the model revealed severe steric clashes in the nonhomologous regions of the filaments. We do note the presence of a small number of filaments (11/556 filaments) containing numerous segments (≥ 10) classified into each type, although the inter-rung steric clashes lend credence to the argument that this results from classification stochasticity instead of the presence of truly mixed filaments.

Overall, these results improve our understanding of the α-synuclein structures underlying MSA and provide a framework for developing therapeutics or diagnostics that bind to MSA filaments with high affinity and selectivity. The existence of multiple MSA α-synuclein folds suggests that these putative molecules should target a conserved region of the filament, as even low-population filament types can predominate if other folds are inhibited. Furthermore, it is possible that Type I_2 filaments may be the major species in certain patients with MSA. Structural analysis on tissue samples from different patients and brain regions will be required to elucidate how MSA filament types are distributed. However, conformation-specific molecules would also be useful for rapidly quantifying each filament type in a tissue sample without needing to resort to cryo-EM [15,33,34]. These molecules should help us continue investigating whether multiple folds may exist in single filaments.

Acknowledgements

Research Center (ADRC) was supported by the National Institutes of Health/National Institute on Aging (AG005134). Portions of the graphical abstract were made using BioRender.com. We thank the patients' families for donating brain tissue.

Conflict of interest

SBP is the founder of Prio Pharma, which did not contribute support to this study. The remaining authors have no conflicts of interest to declare.

Author contributions

NY, DRS, NAP, and GEM designed the research; NY, FC, ET, AM, DAM, and GEM performed experiments; NY, SBP, DRS, NAP, and GEM analyzed the data; NY, DRS, NAP, and GEM wrote the manuscript. All authors read and approved the final manuscript.

Peer review

The peer review history for this article is available at https://www.webofscience.com/api/gateway/wos/peer-review/10.1002/1873-3468.15048.

Data accessibility

Refined atomic models have been deposited in the Protein Data Bank (PDB) under accession numbers 9CD9 (Type II$_2$) and 9CDA (Type I$_2$). Corresponding cryo-EM maps have been deposited in the Electron Microscopy Data Bank (EMDB) with accession numbers EMD-45464 (Type II$_2$) and EMD-45465 (Type I$_2$). Please address requests for materials to the corresponding author.

References

1 Dev KK, Hofele K, Barbieri S, Buchman VL and van der Putten H (2003) Part II: alpha-synuclein and its molecular pathophysiological role in neurodegenerative disease. *Neuropharmacology* **45**, 14–44.

2 Burré J, Sharma M and Südhof TC (2017) Cell biology and pathophysiology of α-synuclein. In Prion Diseases (Prusiner SB, ed.), pp. 277–304. Cold Spring Harbor Laboratory Press, Cold Spring Harbor, NY.

3 Huang M, Wang B, Li X, Fu C, Wang C and Kang X (2019) α-Synuclein: a multifunctional player in exocytosis, endocytosis, and vesicle recycling. *Front Neurosci* **13**, 28.

4 Peelaerts W and Baekelandt V (2016) α-Synuclein strains and the variable pathologies of synucleinopathies. *J Neurochem* **139**, 256–274.

5 Brás IC, Dominguez-Meijide A, Gerhardt E, Koss D, Lázaro DF, Santos PI, Vasili E, Xylaki M and Outeiro TF (2020) Synucleinopathies: where we are and where we need to go. *J Neurochem* **153**, 433–454.

6 Graham JG and Oppenheimer DR (1969) Orthostatic hypotension and nicotine sensitivity in a case of multiple system atrophy. *J Neurol Neurosurg Psychiatry* **32**, 28–34.

7 Papp MI, Kahn JE and Lantos PL (1989) Glial cytoplasmic inclusions in the CNS of patients with multiple system atrophy (striatonigral degeneration, olivopontocerebellar atrophy and Shy-Drager syndrome). *J Neurol Sci* **94**, 79–100.

8 Spillantini MG, Crowther RA, Jakes R, Cairns NJ, Lantos PL and Goedert M (1998) Filamentous α-synuclein inclusions link multiple system atrophy with Parkinson's disease and dementia with Lewy bodies. *Neurosci Lett* **251**, 205–208.

9 Tu PH, Galvin JE, Baba M, Giasson B, Tomita T, Leight S, Nakajo S, Iwatsubo T, Trojanowski JQ and Lee VM (1998) Glial cytoplasmic inclusions in white matter oligodendrocytes of multiple system atrophy brains contain insoluble α-synuclein. *Ann Neurol* **44**, 415–422.

10 Wakabayashi K, Yoshimoto M, Tsuji S and Takahashi H (1998) α-Synuclein immunoreactivity in glial cytoplasmic inclusions in multiple system atrophy. *Neurosci Lett* **249**, 180–182.

11 Prusiner SB, Woerman AL, Mordes DA, Watts JC, Rampersaud R, Berry DB, Patel S, Oehler A, Lowe JK, Kravitz SN *et al.* (2015) Evidence for α-synuclein prions causing multiple system atrophy in humans with parkinsonism. *Proc Natl Acad Sci USA* **112**, E5308–E5317.

12 Woerman AL, Watts JC, Aoyagi A, Giles K, Middleton LT and Prusiner SB (2017) α-Synuclein: multiple system atrophy prions. In Prion Diseases (Prusiner SB, ed.), pp. 319–330. Cold Spring Harbor Laboratory Press, Cold Spring Harbor, NY.

13 Schweighauser M, Shi Y, Tarutani A, Kametani F, Murzin AG, Ghetti B, Matsubara T, Tomita T, Ando T, Hasegawa K *et al.* (2020) Structures of α-synuclein filaments from multiple system atrophy. *Nature* **585**, 464–469.

14 Yang Y, Shi Y, Schweighauser M, Zhang X, Kotecha A, Murzin AG, Garringer HJ, Cullinane PW, Saito Y, Foroud T *et al.* (2022) Structures of α-synuclein filaments from human brains with Lewy pathology. *Nature* **610**, 791–795.

15 Yang Y, Garringer HJ, Shi Y, Lövestam S, Peak-Chew S, Zhang X, Kotecha A, Bacioglu M, Koto A, Takao M *et al.* (2023) New SNCA mutation and structures of α-synuclein filaments from juvenile-onset synucleinopathy. *Acta Neuropathol* **145**, 561–572.

16 Zheng SQ, Palovcak E, Armache JP, Verba KA, Cheng Y and Agard DA (2017) MotionCor2: anisotropic

correction of beam-induced motion for improved cryo-electron microscopy. *Nat Methods* **14**, 331–332.

17 de la Rosa-Trevin JM, Quintana A, Del Cano L, Zaldivar A, Foche I, Gutierrez J, Gomez-Blanco J, Burguet-Castell J, Cuenca-Alba J, Abrishami V *et al.* (2016) Scipion: a software framework toward integration, reproducibility and validation in 3D electron microscopy. *J Struct Biol* **195**, 93–99.

18 He S and Scheres SHW (2017) Helical reconstruction in RELION. *J Struct Biol* **198**, 163–176.

19 Kimanius D, Dong L, Sharov G, Nakane T and Scheres SHW (2021) New tools for automated cryo-EM single-particle analysis in RELION-4.0. *Biochem J* **478**, 4169–4185.

20 Rohou A and Grigorieff N (2015) CTFFIND4: fast and accurate defocus estimation from electron micrographs. *J Struct Biol* **192**, 216–221.

21 Pettersen EF, Goddard TD, Huang CC, Couch GS, Greenblatt DM, Meng EC and Ferrin TE (2004) UCSF chimera—a visualization system for exploratory research and analysis. *J Comput Chem* **25**, 1605–1612.

22 Emsley P, Lohkamp B, Scott WG and Cowtan K (2010) Features and development of Coot. *Acta Crystallogr D Biol Crystallogr* **66**, 486–501.

23 Croll TI (2018) ISOLDE: a physically realistic environment for model building into low-resolution electron-density maps. *Acta Crystallogr D Struct Biol* **74**, 519–530.

24 Adams PD, Afonine PV, Bunkoczi G, Chen VB, Davis IW, Echols N, Headd JJ, Hung LW, Kapral GJ, Grosse-Kunstleve RW *et al.* (2010) PHENIX: a comprehensive Python-based system for macromolecular structure solution. *Acta Crystallogr D Biol Crystallogr* **66**, 213–221.

25 Miake H, Mizusawa H, Iwatsubo T and Hasegawa M (2002) Biochemical characterization of the core structure of α-synuclein filaments. *J Biol Chem* **277**, 19213–19219.

26 Radamaker L, Baur J, Huhn S, Haupt C, Hegenbart U, Schonland S, Bansal A, Schmidt M and Fandrich M (2021) Cryo-EM reveals structural breaks in a patient-derived amyloid fibril from systemic AL amyloidosis. *Nat Commun* **12**, 875.

27 Fitzpatrick AWP, Falcon B, He S, Murzin AG, Murshudov G, Garringer HJ, Crowther RA, Ghetti B, Goedert M and Scheres SHW (2017) Cryo-EM structures of tau filaments from Alzheimer's disease. *Nature* **547**, 185–190.

28 Gremer L, Schölzel D, Schenk C, Reinartz E, Labahn J, Ravelli RBG, Tusche M, Lopez-Iglesias C, Hoyer W, Heise H *et al.* (2017) Fibril structure of amyloid-β(1-42) by cryo-electron microscopy. *Science* **358**, 116–119.

29 Falcon B, Zivanov J, Zhang W, Murzin AG, Garringer HJ, Vidal R, Crowther RA, Newell KL, Ghetti B, Goedert M *et al.* (2019) Novel tau filament fold in chronic traumatic encephalopathy encloses hydrophobic molecules. *Nature* **568**, 420–423.

30 Shi Y, Zhang W, Yang Y, Murzin AG, Falcon B, Kotecha A, van Beers M, Tarutani A, Kametani F, Garringer HJ *et al.* (2021) Structure-based classification of tauopathies. *Nature* **598**, 359–363.

31 Scheres SH, Zhang W, Falcon B and Goedert M (2020) Cryo-EM structures of tau filaments. *Curr Opin Struct Biol* **64**, 17–25.

32 Gilman S, Wenning GK, Low PA, Brooks DJ, Mathias CJ, Trojanowski JQ, Wood NW, Colosimo C, Dürr A, Fowler CJ *et al.* (2008) Second consensus statement on the diagnosis of multiple system atrophy. *Neurology* **71**, 670–676.

33 Condello C, Lemmin T, Stöhr J, Nick M, Wu Y, Watts JC, Oehler A, Keene CD, Bird TD, van Duinen SG *et al.* (2018) Structural heterogeneity and intersubject variability of Aβ in familial and sporadic Alzheimer's disease. *Proc Natl Acad Sci USA* **115**, E782–E791.

34 Shahnawaz M, Mukherjee A, Pritzkow S, Mendez N, Rabadia P, Liu X, Hu B, Schmeichel A, Singer W, Wu G *et al.* (2020) Discriminating α-synuclein strains in Parkinson's disease and multiple system atrophy. *Nature* **578**, 273–277.

Supporting information

Additional supporting information may be found online in the Supporting Information section at the end of the article.

Fig. S1. Structures of MSA filaments reported by Schweighauser et al.

Fig. S2. Flowchart of MSA filament data processing.

Fig. S3. Model of MSA Type II$_2$-I$_2$ mixed cofilament wherein adjacent Type II$_2$ and Type I$_2$ rungs were aligned using residues 57–93 of PF-IIA.

Fig. S4. Representative negative-stain transmission electron micrographs of *ex vivo* MSA filaments.

Fig. S5. Two-dimensional class averages of MSA filaments extracted at two different box sizes.

Fig. S6. Characterization of MSA Type II$_2$ filaments in the dataset.

Fig. S7. Characterization of MSA Type I$_2$ filaments in the dataset.

Table S1. Cryo-EM data collection and model refinement statistics.

Table S2. MSA filament type distribution across different brain regions in different cases.